Acta Geochim (2024) 43:40–58
https://doi.org/10.1007/s11631-023-00639-1

ORIGINAL ARTICLE

Geochemistry, zircon U–Pb geochronology, and Hf isotopes of S-type granite in the Baoshan block, constraints on the age and evolution of the Proto-Tethys

Jianjun Zhang[1,2] · Chuanlong Mou[3] · Chendong Liu[1,2] · Yong Zhang[1,2] · Ting Chen[4] · Hualiang Li[1,2]

Received: 20 April 2023 / Revised: 23 August 2023 / Accepted: 14 September 2023 / Published online: 4 October 2023

Abstract Geochemistry, zircon U–Pb geochronology, and Hf isotope data for the Early Paleozoic granites in the Baoshan Block reveal the Early Paleozoic tectonic evolution of the Proto-Tethys. The samples are high-K, calc-alkaline, strongly peraluminous rocks with A/CNK values of 1.37–1.46, are enriched in SiO_2, K_2O, and Rb, and are depleted in Nb, P, Ti, Eu, and heavy rare earth elements, which indicates the crystallization fractionation of the granitic magma. Zircon U–Pb dating indicates that they formed in ca. 480 Ma. The Nansa granites have $\varepsilon_{Hf}(t)$ values ranging from -16.04 to 4.36 with corresponding T^{C}_{DM} ages of 2.10–0.81 Ga, which suggests the magmas derived from the partial melting of ancient metasedimentary with minor involvement of mantle-derived components. A synthesis of data for the Early Paleozoic igneous rocks in the Baoshan block and adjacent (Tengchong, Qiangtang, Sibumasu, Himalaya, etc.) blocks indicates that these blocks were all aligned along the proto-Tethyan margin of East Gondwana in the Early Paleozoic. The Early Paleozoic S-type granites from Nansa were generated in a high-temperature and low-pressure (HTLP) extensional tectonic setting, which resulted from Andean-type orogeny instead of the final assembly of Gondwana or crustal extension in a non-arc environment. In certain places, an expanding environment may exist in opposition to the tectonic backdrop of the lithosphere's thickening and shortening, leading the crust to melt and decompress, mantle-derived materials to mix, and a small quantity of peraluminous granite to emerge.

Keywords Baoshan block · Early Paleozoic · Granite · Geochemistry · Zircon · Geochronology · Hf isotope

1 Introduction

The West Burma, Baoshan, and Tengchong terranes are located in the south of the eastern Tethys tectonic domain (ETTD), which is a large-scale orogenic zone that stretches between the Indian and Eurasian plates, while the Qiangtang and Lhasa terranes are located in the north (Fig. 1a). As a result of several stages of oceanic subduction, plate convergence, collision, and accretion, the ETTD is covered with a substantial amount of igneous rocks (Wang et al. 2013; Deng et al. 2017). With the assembling of many continental pieces and the commencement of subduction along the Peri-Gondwana edge, the Late Neoproterozoic-Early Paleozoic period is noteworthy (Murphy et al. 2011; Zhu et al. 2012; Meinhold et al. 2013). Yet, the later Cenozoic deformation brought on by the collision of India and Eurasia frequently makes it difficult to unravel the petrogenesis and tectonic backgrounds of these rocks (Pan et al. 2012). Lately, numerous works argued that the Early Paleozoic magmatic rocks were formed by the final assembly of Gondwana (Xu et al. 2014), however, the majority of studies stated that these were formed by

✉ Jianjun Zhang
jianjunzhang87@163.com

[1] Institute of Geological Survey, East China University of Technology, Nanchang 330013, China

[2] School of Earth Sciences, East China University of Technology, Nanchang 330013, China

[3] Chengdu Geological Survey Center, Chengdu 610081, China

[4] School of Water Resources & Environmental Engineering, East China University of Technology, Nanchang 330013, China

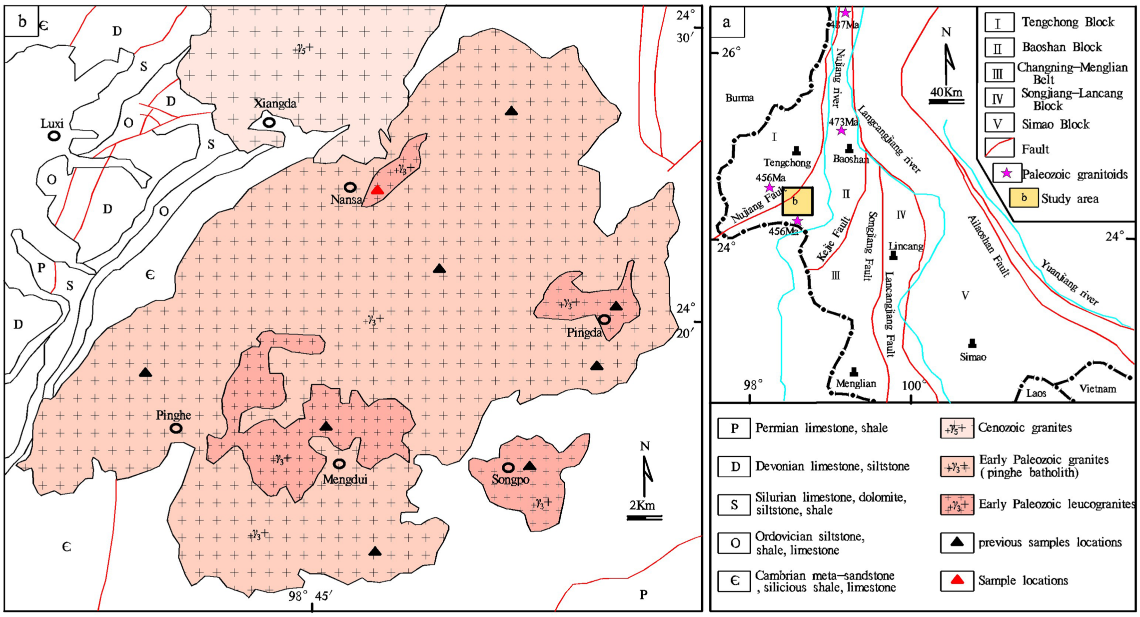

Fig. 1 **a** Generalized tectonic map of the Baoshan block in Western Yunnan Province (Shen et al. 2002), **b** Simplified geological map of the Early Paleozoic granitoids in Baoshan Block

Andean-type orogeny (Wang et al. 2013). Even though past researchers have amassed a wealth of information, more research is required since the Early Paleozoic East Tethyan evolution model cannot be accurately and entirely constructed with the current understanding. To attempt to solve these issues, more support from geochemical, geochronological, and isotopic geological analyses of Early Paleozoic magmatic groups is necessary, as stated previously. We investigate the granites found in the Baoshan block and present new geochemical and geochronological data such as petrography, whole-rock geochemistry, zircon U–Pb ages, and zircon Hf isotopic data since the Baoshan block is an important branch of the ETTD. Through an investigation of the petrogenesis and tectonic settings of Early Paleozoic granites, the tectonic evolution of western Yunnan and its relationship with the Gondwana supercontinent are discussed.

2 Geological background and petrography

The Nujiang-Longling-Luxi fault to the west and the Kejie-Nandinghe fault to the east border the Baoshan block, which is located in the midst of the Tibet-Yunnan-Thailand-Malaysia plate (Fig. 1b). The principal argument for relocating the Baoshan block to the northern boundary of Gondwana during the Cisuralian is the presence of diamictites and cool-water fossils with Gondwana affinities (Wopfner 1996; Metcalfe 2013). The Gongyanghe Group, the earliest sedimentary series in the Baoshan block, is formed of metamorphosed volcano-sedimentary rocks, tonalite, and gabbro with no Early Paleozoic deposits (Yang et al. 2012). Late Precambrian, Early Paleozoic, Middle Permian, Late Triassic, and Cretaceous granites are the principal intermediate-felsic intrusions in the Baoshan block (Dong et al. 2013b; Li et al. 2015a). The majority of the Late Precambrian granitic rocks are exposed in the Laojiezi and Zhibenshan regions, with ages of 645 and 687 Ma, respectively (Zhang et al. 1990; Li et al. 2010a). The Early Paleozoic peraluminous granitoids, which largely occur in the Shuangmaidi and Pinghe districts, have been dated 502–448 and 468–447 Ma, respectively (Wang et al. 2013; Li et al. 2015a, 2016a). The Muchang pluton (ca. 266 Ma) represents the Middle Permian A-type granites that were emplaced in the south half of the Baoshan block (Ye et al. 2010). The Late Triassic S-type granites (about 231 Ma) were deposited on the eastern margin of the Baoshan block (Nie et al. 2012). The Zhibenshan pluton represents the Early Cretaceous S-type granites (ca. 127 Ma). The Huataolin pluton represents Cenozoic granite (ca. 100–60 Ma) (Jin and Zhuang 1988; Chen et al. 2008).

The Pinghe batholith is the largest granitoid intrusion in the Baoshan block, comprising an estimated outcrop area of approximately 800 km^2 (Fig. 1b). Granite and monzogranite are the primary lithologies of the Pinghe Batholith. The mineral content, structure, and structure of the rock are rather uniform. The lithology of the edge is somewhat transitional to neutral granodiorite, although no lithofacies zoning is seen. The Nansa pluton is an intrusion of the Pinghe batholith. According to a field study, the lithology of the Nansa pluton is leucogranite, which differs from the

Pinghe batholiths (Fig. 2a). They are made up of anhedral granular quartz (31%–43%), subhedral K-feldspar (23%–32%), subhedral and platy plagioclase (24%–34%), with mild sericitization in the center area, 3%–8% muscovite, and 2%–3% biotite. Biotite is the most common ferromagnesian phase. Zircon, apatite, magnetite, and ilmenite are examples of accessory minerals (Fig. 2b).

3 Analytical methods

3.1 Whole-rock major and trace elements

Before examination, bulk materials were crushed to 200 mesh using an agate mill. Major element oxides were evaluated using a wavelength X-ray fluorescence (XRF) spectrometer at the Research Center of Analyses, Beijing Research Institute of Uranium Geology, Beijing, China, with analytical errors of less than 5%. The gravimetric technique was used to calculate the LOI. In the Central Laboratory of Mineral Resources, Institute of Geology and Geophysics of the Chinese Academy of Sciences in Beijing, China, trace element compositions were determined using a Finnigan MAT Element mass spectrometer. Liu et al. (2008) describe the entire analytical technique. Indium was employed as an internal standard for matrix effects and instrument drift correction. Regular studies of standards with a 10% frequency were used to manage measurement error and drift. The uncertainties measured at the ppm level are less than 3%–10% for trace elements and 5%–10% for REE.

3.2 LA-ICP-MS zircon U–Pb dating

Zircon grains for U–Pb dating were purified by handpicking under a binocular microscope after being separated using conventional density and magnetic separation techniques. Zircons that had been separated were mounted in epoxy resin, polished to half their thickness, covered in gold, and captured in both transmitted and reflected light for photography. Before U–Pb isotopic analyses, each grain's internal structure was analyzed using cathodoluminescence (CL) imaging via a scanning electron microprobe.

LA-ICP-MS was used to conduct U–Pb dating and trace element analyses of zircon at the key laboratory for the study of focused magmatism and giant ore deposits, the China Geological Survey Xi'an Geological Survey Center. A Geo Las Pro was used for laser sampling. Ion-signal intensities were measured using an Agilent 7700 × ICP-MS instrument. As a carrier gas, helium was used. Argon was used as a make-up gas and was mixed with the carrier gas before entering the ICP via a T-connector. Each analysis included a 10-s background acquisition (gas blank) followed by a 40-s data acquisition from the sample.

Each individual analysis was collected using the Agilent Chemstation. Glitter 4.4 performed offline selection and integration of background and analyte signals, as well as time-drift correction and quantitative calibration for trace element analyses and U–Pb dating. The instrumentation and data acquisition procedures are similar to those described by Li et al. (2015a, b, c).

The external standard for U–Pb dating was Zircon 91,500. A linear interpolation was used to correct time-dependent drifts in U-Th-Pb isotopic ratios with time. The uncertainty of preferred values for the external standard 91,500 was propagated to the sample results. Isoplot/Ex

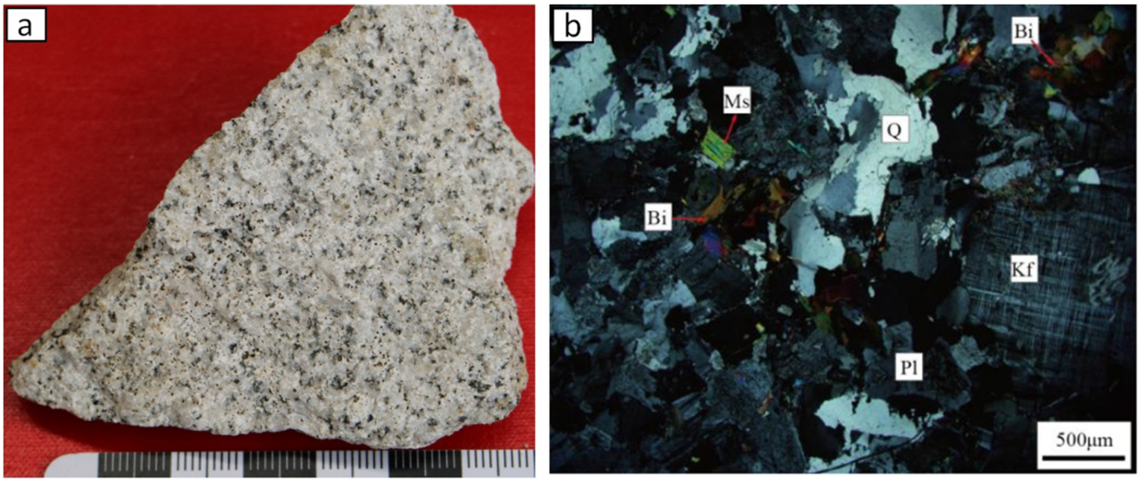

Fig. 2 Outcrop and micrographic photos of representative granitic samples from the Nansa area in the Baoshan block, SW China. Q: quartz, Kf: K-feldspar, Pl: plagioclase, Ms: Muscovite, Bi: biotite

version 3 was used to create Concordia diagrams and weighted mean calculations (Ludwig 2003). Zircon trace element compositions were calibrated against reference materials (NIST610) and Si as internal standardization. The GeoReM database was used to determine the preferred element concentrations for the NIST reference glasses.

3.3 Hf isotope analyses

At the key laboratory for the study of focused magmatism and giant ore deposits, MLR, in the Xi'an Center of Geological Survey, China Geological Survey, in situ zircon Hf isotope analyses were performed using a Geolas Pro laser-ablation system coupled to a Neptune multiple-collector ICP-MS. The instrumentation and data acquisition procedures are similar to those described by Meng et al. (2014). For the analyses, a stationary laser ablation spot with a beam diameter of 30 μm was used. Helium was used to transport the ablated aerosol, which was then mixed with argon in a mixing chamber before being introduced to the ICP-MS plasma. All of the Hf analyses were performed at the same locations for U–Pb laser ablation. During this study, the reference standard was zircon GJ-1, which produced a weighted mean $^{176}Hf/^{177}Hf$ ratio of 0.282030 (2 SE).

4 Results

4.1 Major and trace elements

The SiO_2 and Al_2O_3 compositions of the samples are 69.80–71.15% and 15.98–16.83%, respectively (Table 1), which is consistent with the Pinghe plutonic batholith (Liu et al. 2009; Dong et al. 2012, 2013b). As a result, they are cited in this study for analysis. The samples are displayed on the total alkalis versus SiO_2 (TAS) diagram in the granite field (Fig. 3). The samples are calc-alkaline, as indicated in the $Na_2O + K_2O$-CaO versus SiO_2 diagram (Fig. 4), magnesian to ferroan, and moderately peraluminous, with an A/CNK range of 1.37–1.46 (Fig. 5). The FeO^T, MgO, and REE levels are extremely low. These traits of the granites are similar to those of the leucogranites that are found in the high Himalayas and other collisional orogens (Vidal et al. 1982; Simon and Nigel 1993; Guo and Li 2009). These rocks have high Rb/Sr ratios but low Ce, Y, Ga, and REE concentrations, which is typical of S-type granite.

Figure 6a shows chondrite-normalized REE patterns and a spider diagram of the samples. Similar patterns can be seen in the chondrite normalized REE patterns of the four different rock types, which show enriched LREE and relatively depleted HREE. Their Eu anomalies are likewise roughly the same, with δEu [$\delta Eu = Eu_N/(Sm_N \times Gd_N)^{1/2}$] between 0.47 and 0.69. REE content ranges from 136.15 to 148.42 ppm. The LREE/HREE values are between 4.63 and 5.47. All of the samples exhibit negative anomalies of Ba, Nb, Sr, and, to a lesser extent, Hf in the primitive-mantle-normalized trace element patterns (Fig. 6b).

4.2 Zircon U–Pb age

The zircon grains in sample LX-27 are mostly subhedral to euhedral, with prismatic shapes (80–200 m long) and an aspect ratio of 1:1–4:1. In CL pictures, they are translucent, colorless to pale brown, and show evident magmatic oscillatory zoning (Fig. 7). Twenty-five analytical spots from LX-27 yielded a wide range of uranium (183–1535 ppm) and thorium (70–356 ppm) contents, with Th/U ratios ranging from 0.2 to 0.6 (Table 2), indicating a magmatic origin (Hoskin and Schaltegger 2018). Twenty-five examinations of these sites resulted in a weighted mean $^{206}Pb/^{238}U$ age of 480.1 ± 4.4 Ma (MSWD = 0.63, Fig. 8), which we interpreted as the granite's crystallization age.

4.3 Zircon Hf isotopes

Table 3 shows the determined values for zircon Hf isotopes. Twenty-five spot studies for zircon from sample LX-27 revealed $^{176}Lu/^{177}Hf$ and $^{176}Hf/^{177}Hf$ ratios of 0.000977–0.004325 and 0.282318–0.282895, respectively, showing that ^{176}Hf has low radiogenic growth. They have $f_{Lu/Hf}$ ratios ranging from − 0.97 to − 0.87, with a concentration between − 0.96 and − 0.95, which is significantly lower than the mafic crust (− 0.34) (Amelin et al. 2000) and sialic crust (− 0.72) (Vervoort and Patchett 1996). T^C_{DM} ages range from 0.81 to 2.10 Ga, with the majority of them falling between 1.71 and 1.98 Ga. The computed $\varepsilon_{Hf}(t)$ values range from − 16.04 to − 1.33, with one exception of 4.36. The $\varepsilon_{Hf}(t)$ values of these Early Paleozoic granites in this study are within those of the already reported ca. 500 to 450 Ma peraluminous granites in the Baoshan block (Chen et al. 2008; Liu et al. 2009; Dong et al. 2012, 2013b; Wang et al. 2013). Inherited and xenocrystic zircons in the granites from the Shuangmaidi and Mengmao areas in the Baoshan block with $^{206}Pb/^{238}U$ ages of ca. 540 to 480 Ma have much varied $\varepsilon_{Hf}(t)$ values from − 11.1 to + 13.5. Other older (> 550 Ma) inherited cores and xenocrysts show varied $\varepsilon_{Hf}(t)$ values and T^C_{DM} ages (Dong et al. 2012). For instance, the Neoproterozoic (955–565 Ma) inherited grains mainly display positive $\varepsilon_{Hf}(t)$ values of 0.3 to 9.5 with T^C_{DM} ages of 1645 to 1150 Ma (Li et al. 2016a). Overall, the Hf isotopic results for zircon from the granitic batholith show that it originated from the Paleo-Mesoproterozoic crust.

Table 1 Whole-rock major, trace element data of the Early Paleozoic granites in the Baoshan Block, western Yunnan

Samples	LX-28	LX-29	LX-31	LX-32
SiO_2	69.95	69.80	71.15	70.81
TiO_2	0.23	0.22	0.19	0.22
Al_2O_3	16.53	16.83	15.98	16.02
$Fe_2O_3{}^T$	2.37	2.34	2.34	2.42
FeO	1.90	1.80	1.85	1.96
MnO	0.06	0.06	0.05	0.05
MgO	1.24	0.88	1.15	0.91
CaO	1.51	1.22	1.58	1.34
Na_2O	3.18	2.92	2.27	3.01
K_2O	3.79	4.18	4.11	3.98
P_2O_5	0.11	0.07	0.10	0.07
LOI	0.97	1.41	1.05	1.37
CIPW normative minerals (wt.%)				
Q	31.36	32.66	36.71	33.29
An	6.64	5.23	6.91	5.85
Ab	27.10	24.88	19.27	25.63
Or	22.64	25.06	24.57	23.82
C	4.88	5.75	5.39	4.73
Hy	6.12	5.03	5.86	5.46
Il	0.44	0.43	0.36	0.41
Mt	0.42	0.53	0.45	0.39
Ap	0.27	0.16	0.25	0.18
Di	81.10	82.60	80.55	82.74
Trace elements (ppm)				
La	28.76	28.46	28.46	26.24
Ce	54.99	54.72	56.88	51.96
Pr	6.70	6.92	6.80	6.42
Nd	25.24	26.15	25.67	24.25
Sm	5.54	5.78	5.41	5.15
Eu	0.85	0.97	1.02	1.09
Gd	5.44	5.41	4.75	4.58
Tb	1.03	0.98	0.88	0.84
Dy	6.85	6.31	6.15	5.72
Ho	1.54	1.35	1.36	1.21
Er	4.70	4.06	4.10	3.59
Tm	0.80	0.68	0.69	0.59
Yb	5.18	4.42	4.49	3.89
Lu	0.81	0.71	0.71	0.62
Y	41.00	35.73	35.05	30.64
Zr	99.09	103.68	98.70	107.30
Zn	41.47	66.87	34.46	63.23
V	32.51	30.48	30.15	27.18
Th	15.82	13.84	15.59	13.23
Pb	32.85	41.29	29.88	41.79
Sc	7.67	6.71	7.16	7.39
Sr	66.33	58.13	57.32	55.57
Rb	202.10	188.00	187.80	232.00
Ni	4.86	4.90	5.82	6.09
Nb	10.03	9.31	9.00	8.18
Cr	14.15	11.98	13.36	13.34
Co	4.61	3.95	4.27	3.99
Cu	3.38	13.61	3.56	13.23
Ba	527.70	598.10	450.31	535.96

Table 1 continued

Samples	LX-28	LX-29	LX-31	LX-32
Hf	2.28	2.13	2.39	2.24
U	2.77	2.47	3.92	3.31
Ta	1.60	1.43	1.71	1.53
K_2O/Na_2O	1.19	1.43	1.81	1.32
SI	11.90	8.72	11.87	9.01
AR	2.09	1.96	1.70	2.06
A/CNK	1.37	1.46	1.45	1.37
A/MF	2.67	3.20	2.70	2.95
C/MF	0.44	0.42	0.48	0.45
CaO/Na_2O	0.47	0.42	0.70	0.45
Al_2O_3/TiO_2	72.82	76.13	84.55	74.51
Rb/Sr	3.05	3.23	3.28	4.17
Rb/Ba	0.38	0.31	0.42	0.43
$(La/Yb)_N$	3.99	4.62	4.55	4.84
$\sum$REE	148.42	146.92	147.36	136.15
LREE/HREE	4.63	5.14	5.37	5.47
Eu/Eu*	0.47	0.53	0.61	0.69
Ce/Ce*	0.97	0.96	1.00	0.98
$(Na_2O + K_2O)/CaO$	4.62	5.82	4.04	5.22
FeO^T/MgO	1.75	2.41	1.85	2.41
HFSE	205.11	203.44	199.63	198.08
Gd_N/Yb_N	0.61	0.71	0.61	0.68

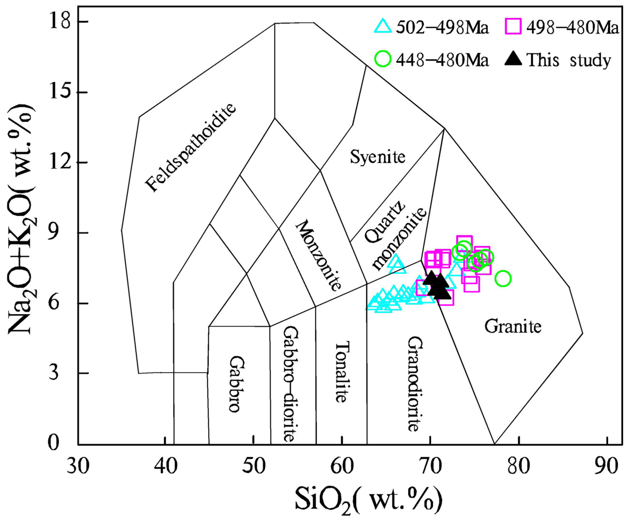

Fig. 3 The TAS classification diagram of the Early Paleozoic granites in the Baoshan block, SW China (Middlemost 1994). Previous data on the Pinghe granites are from Liu et al. (2009) and Dong et al. (2012, 2013b)

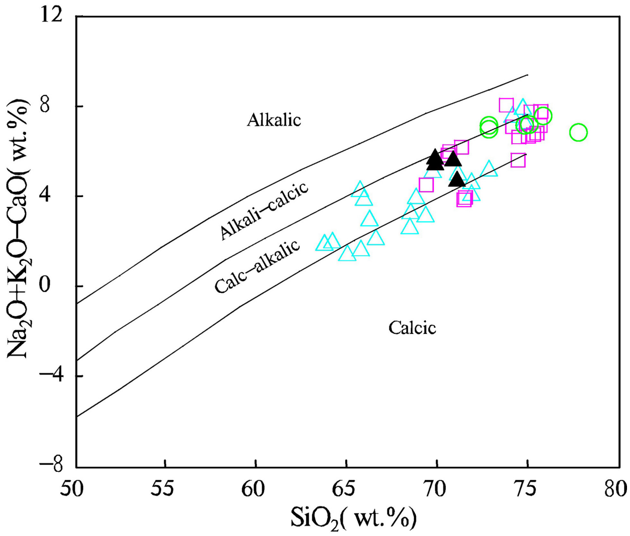

Fig. 4 Modified alkali-line index ($Na_2O + K_2O–CaO$) versus SiO_2 diagram of the Early Paleozoic granites in the Baoshan block, SW China (Frost et al. 2001), Symbols are the same as those in Fig. 3

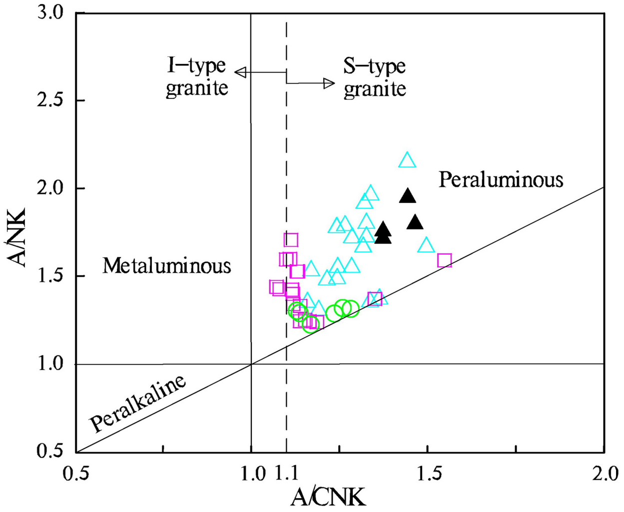

Fig. 5 Molar Al/(Na + K) vs. Al/(Ca + Na + K) diagram of the Early Paleozoic granites in the Baoshan block, SW China (Maniar and Piccoli 1989). Symbols are the same as those in Fig. 3

5 Discussion

5.1 Early Paleozoic magmatism

The two-mica granites from Zhibenshan and the peraluminous granites from the Shuangmaidi were deposited to the north of the Baoshan block at around 473 and 470–459 Ma, respectively (Chen 1987). The Mengmao granites in the center of the Baoshan block have been dated to between 480 and 455 Ma (Xiong et al. 2012). Leucogranite from the Pinghe Formation and monzogranite from the same batholiths were both deposited to the south of the Baoshan block at approximately 476–448 and 502–466 Ma, respectively (Liu et al. 2009; Dong et al. 2013b; Wang et al. 2013). According to the geochronological evidence presented here, the Nansa granitics were produced around 480 Ma. These findings show that the Baoshan block experienced Early Paleozoic magmatism between 502 and 448 Ma. Some continental blocks also include Early Paleozoic magmatism. The Tengchong block's granitic gneiss has produced zircon U–Pb ages of approximately 456 Ma (Cong et al. 2010) and approximately 518–484 Ma (Li et al. 2011; Cai et al. 2013). In the Sibumasu block of the Upper Peninsula of Thailand, the Khao Tao orthogneiss formed around 502 Ma (Lin et al. 2013) and the Khao Dat Fa granite formed in 477 Ma (Kawakami et al. 2014). Zircon U–Pb dating in the Western Qiangtang (476–471 Ma) (Pullen et al. 2011), Amdo (530–470 Ma) (Jerome et al. 2012), and Tethyan Himalaya (530–470 Ma) (Cawood and Buchan 2007; Quigley et al. 2008) have also revealed the presence of Early Paleozoic magmatic rocks. The current research on tectonomagmatic records suggests that these blocks, together with the Baoshan block, were all oriented along the proto-Tethyan border of East Gondwana in the Early Paleozoic (Metcalfe 2006, 2013), implying that Early Paleozoic magmatism was substantially developed along the peri-Gondwana frontier.

5.2 Petrogenesis

5.2.1 Petrogenetic type

Chappell and White (1974, 1992) proposed the S-I classification for granites, which later evolved into the "alphabet classification" of S-, I-, M-, and A-type granites. The samples differ from M-type granites, which typically have K_2O contents of less than 1 wt.%, by having high K_2O

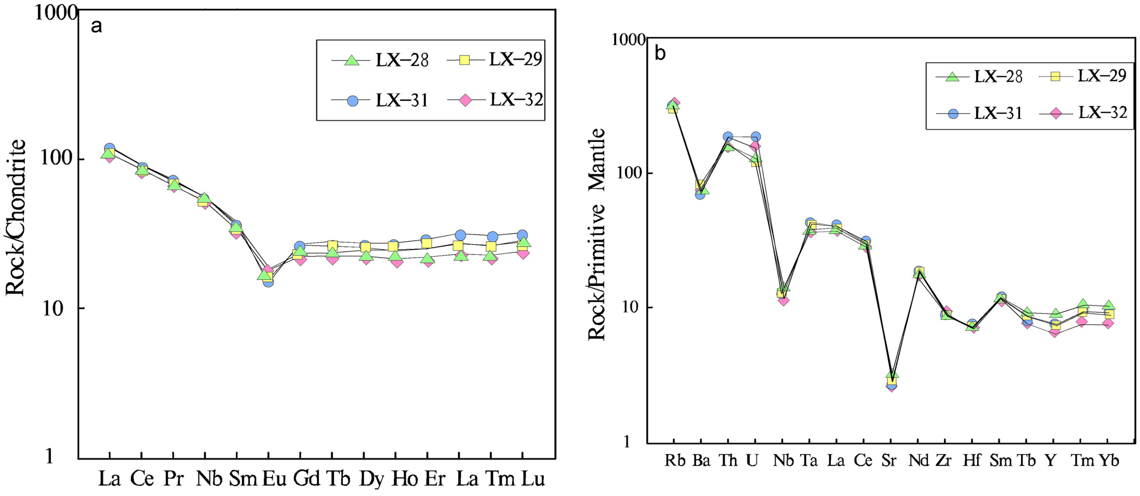

Fig. 6 **a** Primitive mantle-normalized trace element spidergram and **b** chondrite-normalized REE patterns of the Nansa granites in the Baoshan block, SW China (Sun and McDonough 1989)

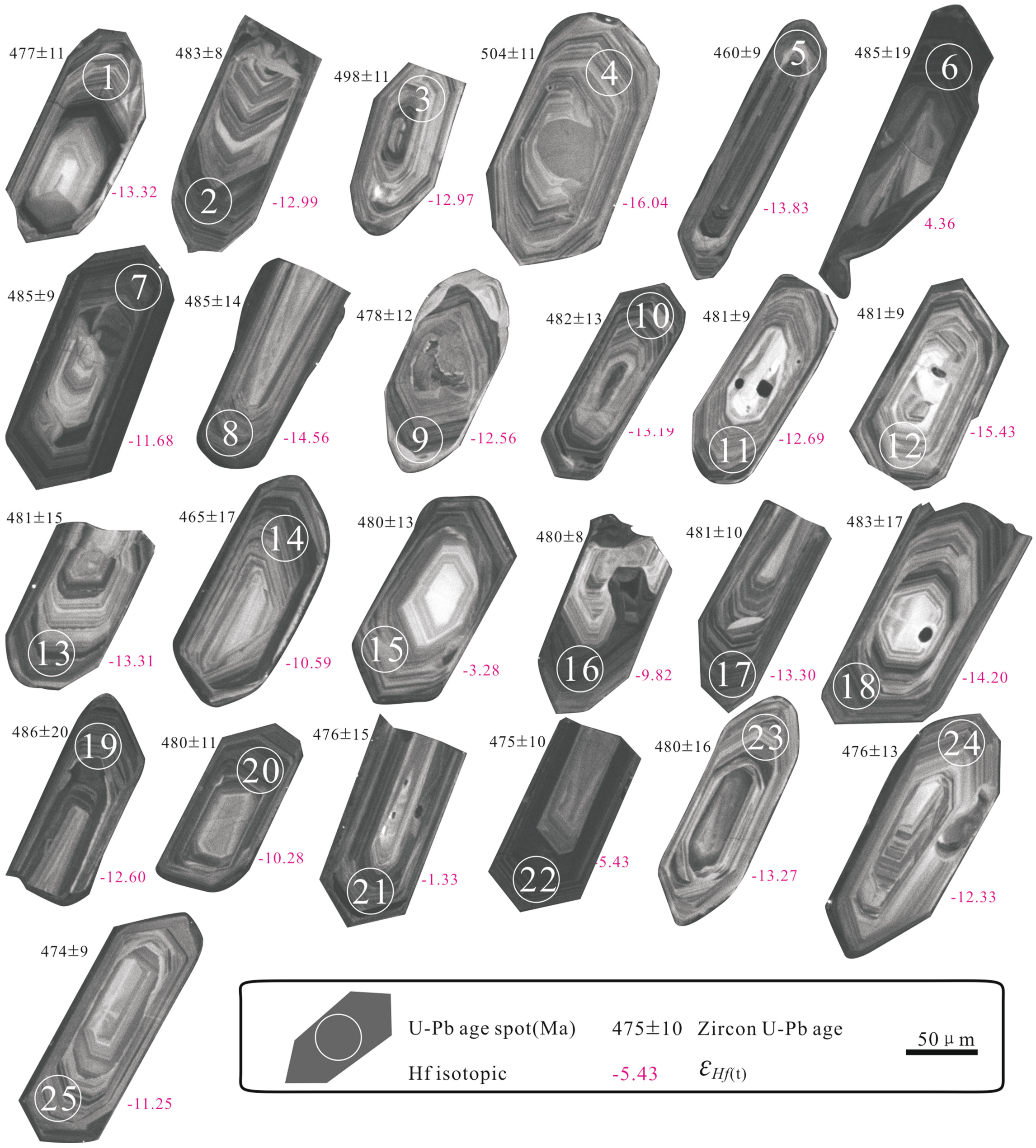

Fig. 7 Cathodoluminescence (CL) electron micrographs of representative zircons separated from the Nansa granites in the Baoshan block, SW China. Spots are analyses of in-situ U–Pb and Hf isotopes

contents of 3.79–4.18 wt.% (Bonin 2007). The SiO_2 contents of 69.80–71.15 wt.%, A/CNK ratios of 1.37–1.46, and normative-CIPW corundum contents of 4.73–5.75 wt.% of the Nansa granitic rocks are similar to S-type granites other than A- and I-type granites (Clemens 2003). For the following two reasons, we rule out the likelihood that they are A-type: In all the granites we have evaluated, hereditary zircon cores are prevalent (Fig. 7), but they are uncommon in A-type granites (Li et al. 2010b); in addition, they all have low $(Na_2O + K_2O)/CaO$ ratios (4.04–5.82), FeO^T/MgO ratios (1.75–2.41), and HFSE contents (Zr + Nb + Ce + Y = 198.08–205.11 ppm) (Whalen et al. 1987; Eby 1990) (Fig. 9a–c). They are less likely to be I-type granites, which are predominantly metaluminous with A/CNK ratios typically < 1.1 (Bruce et al. 2012). These samples are classified as S-type granites on the $(Al_2O_3\text{-}(K_2O + Na_2O)\text{-}CaO\text{-}(FeO^T + MgO)$ discrimination diagrams (Fig. 9d).

5.3 Fractional crystallization

The spidergrams show substantially negative Ba, Sr, Eu, P, Nb, and Ti anomalies as well as a decrease in MgO and

Table 2 LA-ICP-MS U–Pb data of the Nansa granites in the Baoshan block, SW China

Isotope ratios												Age(Ma)					
No	U(ppm)	Th(ppm)	Pb(ppm)	Th/U	$^{238}U/^{232}Th$	$^{207}Pb/^{206}Pb$	1σ	$^{207}Pb/^{235}U$	1σ	$^{206}Pb/^{238}U$	1σ	$^{207}Pb/^{206}Pb$	1σ	$^{207}Pb/^{235}U$	1σ	$^{206}Pb/^{238}U$	1σ
1	289	105	115	0.4	2.7522	0.0567	0.0051	0.6001	0.0527	0.0768	0.0018	478	188	477	33	477	11
2	959	356	344	0.4	2.6923	0.0569	0.0032	0.6094	0.0335	0.0778	0.0014	485	120	483	21	483	8
3	476	297	197	0.6	1.6026	0.0571	0.0048	0.6320	0.0521	0.0803	0.0019	496	177	497	32	498	11
4	299	125	119	0.4	2.3876	0.0574	0.0048	0.6433	0.0521	0.0813	0.0019	506	173	504	32	504	11
5	598	236	214	0.4	2.5360	0.0562	0.0038	0.5728	0.0382	0.0739	0.0015	460	145	460	25	460	9
6	1004	336	373	0.3	2.9918	0.0526	0.0088	0.5665	0.0928	0.0781	0.0031	313	342	456	60	485	19
7	432	142	159	0.3	3.0517	0.0569	0.0039	0.6122	0.0413	0.0781	0.0016	486	146	485	26	485	9
8	525	160	190	0.3	3.2869	0.0570	0.0065	0.6139	0.0685	0.0781	0.0023	491	235	486	43	485	14
9	306	103	111	0.3	2.9723	0.0615	0.0061	0.6520	0.0628	0.0769	0.0021	656	199	510	39	478	12
10	231	85	89	0.4	2.7002	0.0575	0.0065	0.6158	0.0674	0.0777	0.0022	511	229	487	42	482	13
11	415	110	151	0.3	3.7631	0.0569	0.0039	0.6072	0.0404	0.0775	0.0015	485	144	482	26	481	9
12	573	204	206	0.4	2.8010	0.0568	0.0037	0.6071	0.0385	0.0775	0.0015	483	138	482	24	481	9
13	251	96	96	0.4	2.6005	0.0568	0.0075	0.6067	0.0783	0.0775	0.0026	483	269	481	49	481	15
14	1535	319	510	0.2	4.8072	0.0538	0.0083	0.5539	0.0838	0.0747	0.0028	361	316	448	55	465	17
15	896	223	317	0.2	4.0144	0.0555	0.0062	0.5906	0.642	0.0772	0.0022	430	231	471	41	480	13
16	686	218	243	0.3	3.1399	0.0568	0.0031	0.6058	0.0324	0.0773	0.0014	483	117	481	20	480	8
17	907	351	322	0.4	2.5816	0.0567	0.0041	0.6052	0.0429	0.0774	0.0016	479	154	481	27	481	10
18	779	205	278	0.3	3.8075	0.0574	0.0082	0.6161	0.0857	0.0778	0.0028	507	287	487	54	483	17
19	848	204	332	0.2	4.1591	0.0589	0.0103	0.6359	0.1077	0.0783	0.0034	564	340	500	67	486	20
20	527	204	188	0.4	2.5824	0.0567	0.0052	0.6040	0.0541	0.0773	0.0019	478	192	480	34	480	11
21	313	150	118	0.5	2.0962	0.0566	0.0073	0.5991	0.0750	0.0767	0.0025	476	262	477	48	476	15
22	398	173	147	0.4	2.3079	0.0566	0.0042	0.5976	0.0430	0.0765	0.0016	477	156	476	27	475	10
23	277	118	102	0.4	2.3398	0.0567	0.0079	0.6048	0.0823	0.0773	0.0027	481	282	480	52	480	16
24	183	70	72	0.4	2.6327	0.0567	0.0065	0.5990	0.0675	0.0767	0.0022	477	237	477	43	476	13
25	352	127	129	0.4	2.7668	0.0565	0.0037	0.5949	0.0386	0.0763	0.0015	473	141	474	25	474	9

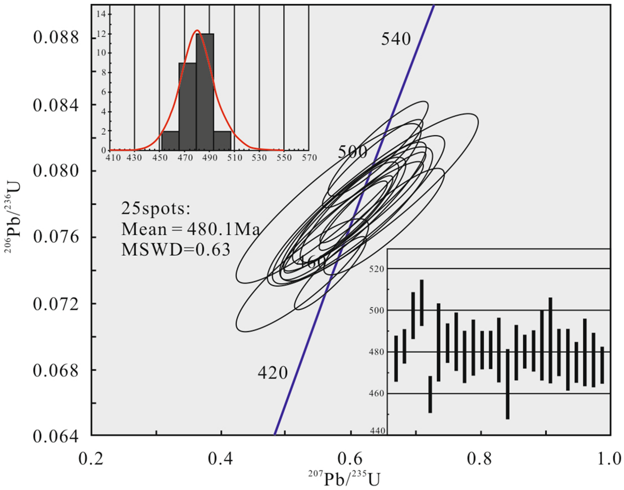

Fig. 8 Concordia diagrams of zircon U–Pb data of representative zircons separated from the Nansa granites in the Baoshan block, SW China

Fe_2O_3, indicating that advanced fractional crystallization was active during the magmatic evolution (Table 2; Fig. 8a,b). MgO and FeO^T levels dropping during magmatic evolution suggest that ferromagnesian minerals (biotite and hornblende) were separated during crystallization. Substantial Ba, Sr, and Eu depletion necessitates significant plagioclase and/or K-feldspar fractionation (Wu et al. 2003; Li et al. 2015b). The strong positive association between Sr and Ba and Eu/Eu* and the weak negative correlation between Sr and Rb support the significant removal of plagioclase and K-feldspar (Fig. 10a–c). The fractionation of apatite produced the significant negative P anomaly (Zhang et al. 2019). The negative Nb and Ti anomalies were attributed to fractionation of the Ti-bearing phase (e.g., ilmenite) (Liu et al. 2018). Accessory minerals have primarily regulated the REE distribution. Further support for the fractionation of apatite, which preferentially incorporates medium REE from the remaining silicate melt, can be provided by the Nansa granites' low $(Gd/Yb)_N$ content (0.61–0.71) (Prowatke and Klemme 2006). The graph of $(La/Yb)_N$ vs. La (Fig. 10d) and the drop in REE in all samples support the considerable elimination of monazite (less than 1%) and allanite.

5.3.1 Nature of source rocks

Typically, the petrogenesis of peraluminous granites is illustrated by fractionation of aluminous-poor magma or derivation from crustal rocks with metapelite and metaigneous components (Clemens 2003). Upper crust granites frequently have low Eu/Eu* ratios (< 1.0), high Th (> 10 ppm), Pb (> 20 ppm), and U (> 2 ppm). The Nansa granites have atypically high Th (13.23–15.82 ppm), Pb (29.88–41.29 ppm), and U (2.47–3.92 ppm), as well as low Eu/Eu* ratios (0.47–0.69), which shows that the source rocks of the granite were derived from the upper crustal materials. These anomalously high Th, Pb, and U values contrast with the general characteristics of the granite researched by Rudnick and Fountain (1995).

According to experiments, extremely peraluminous granites formed from pelitic rocks with a high clay content and little plagioclase have a CaO/Na_2O ratio (< 0.3) that is much lower than that of meta-igneous rocks and psammitic rocks with a high plagioclase content and a CaO/Na_2O ratio (> 0.3). The samples show a preference for psammite-derived melt because of their high CaO/Na_2O ratios of 0.42–0.70 and low Al_2O_3/TiO_2 ratios of 72.82–84.55 (Fig. 11a). The Rb–Sr-Ba variations in exceedingly peraluminous granites have been used to decipher source properties (Sylvester 1998). The Nansa granites are at the melt endmember derived from psammite and have low Rb/Sr and Rb/Ba ratios, which are within the ranges for clay-poor sources (Fig. 11b).

The Hf isotope of zircon in magmatic rocks has been successfully used for source rock tracking. In general, juvenile crustal material formed by differentiation of mantle material and mantle-derived rocks have high $\varepsilon_{Hf}(t)$ values and $^{176}Hf/^{177}Hf$ ratios in zircons, whereas crust or crust-contaminated zircons have lower $\varepsilon_{Hf}(t)$ values and $^{176}Hf/^{177}Hf$ ratios (Kinny 2003; Shen et al. 2009). Except for one outlier of 4.36, the $\varepsilon_{Hf}(t)$ values of the samples range from − 16.04 to − 1.33 and are somewhat higher than those of the S-type granitoids, which were assumed to arise almost exclusively from crustal basement in the Baoshan block (Dong et al. 2013b) and point near the chondrite evolution line and the lower crust region (Fig. 12), suggesting that the source magma of the Nansa granites were generated from the ancient crust with minimal mantle melts being added. Zircons' $\varepsilon_{Hf}(t)$ values of 4.36 give some indication of the contributions made by melts coming from the mantle (Li et al. 2016b). The T^C_{DM} dates of the rocks range from 0.81 to 2.10 Ga, indicating that the ancient crust originated during the Paleo-Mesoproterozoic period.

5.4 Tectonic implications

5.4.1 Tectonic significance

Flat HREE patterns ($Gd_N/Yb_N = 0.61–0.71$) and high Y (30.64–41.00 ppm) and Yb (Yb = 3.89–5.18 ppm) contents show that the samples lack residual garnet, which persists at pressures of 0.5 GPa (Wang et al. 2012). The samples on the ($Al_2O_3 + Fe_2O_3^T + MgO + Ti_2O$) versus $Al_2O_3/(Fe_2O_3^T + MgO + Ti_2O)$ diagram (Fig. 13a) were made experimentally at pressures plotted within the LP reaction field that corresponded to pressures less than 5

Table 3 Hf isotopic data of zircon grains from the Early Paleozoic granites in the Baoshan block, SW China

No	*Age(Ma)*	$^{176}Yb/^{177}Hf$	$^{176}Lu/^{177}Hf$	$^{176}Hf/^{177}Hf$	2σ	Hf_i	$\varepsilon_{Hf}(t)$	1σ	T_{DM}(Ga)	1σ	T^C_{DM}(Ga)	1σ	$f_{Lu/Hf}$
1	477	0.046231	0.001087	0.282395	0.000029	0.282395	−13.32	1.01897	1.21	0.04088	1.93	0.04088	−0.97
2	483	0.057378	0.001319	0.282405	0.000022	0.282405	−12.99	0.76356	1.21	0.03083	1.90	0.03083	−0.96
3	498	0.060875	0.001443	0.282405	0.000028	0.282405	−12.97	0.98245	1.21	0.03980	1.90	0.03980	−0.96
4	504	0.041368	0.000977	0.282318	0.000026	0.282318	−16.04	0.92081	1.32	0.03677	2.10	0.03677	−0.97
5	460	0.058151	0.001304	0.282381	0.000023	0.282381	−13.83	0.82134	1.24	0.03313	1.96	0.03313	−0.96
6	485	0.188848	0.004325	0.282895	0.000022	0.282895	4.36	0.76987	0.56	0.03424	0.81	0.03424	−0.87
7	485	0.064668	0.001496	0.282442	0.000025	0.282442	−11.68	0.86479	1.16	0.03512	1.82	0.03512	−0.95
8	485	0.038041	0.000888	0.282360	0.000022	0.282360	−14.56	0.76788	1.26	0.03062	2.00	0.03062	−0.97
9	478	0.045138	0.001059	0.282417	0.000025	0.282417	−12.56	0.88764	1.18	0.03561	1.88	0.03561	−0.97
10	482	0.044322	0.001065	0.282399	0.000027	0.282399	−13.19	0.94842	1.21	0.03804	1.92	0.03804	−0.97
11	481	0.049501	0.001210	0.282413	0.000032	0.282413	−12.69	1.12519	1.19	0.04531	1.89	0.04531	−0.96
12	481	0.044899	0.001068	0.282336	0.000026	0.282336	−15.43	0.89250	1.30	0.03574	2.06	0.03574	−0.97
13	481	0.057071	0.001316	0.282396	0.000027	0.282396	−13.31	0.94975	1.22	0.03834	1.93	0.03834	−0.96
14	465	0.072978	0.001730	0.282473	0.000023	0.282473	−10.59	0.80248	1.12	0.03282	1.75	0.03282	−0.95
15	480	0.131161	0.002974	0.282679	0.000025	0.282679	−3.28	0.88431	0.86	0.03762	1.29	0.03762	−0.91
16	480	0.071380	0.001618	0.282494	0.000023	0.282494	−9.82	0.78791	1.09	0.03215	1.71	0.03215	−0.95
17	481	0.058060	0.001332	0.282396	0.000022	0.282396	−13.29	0.75397	1.22	0.03045	1.92	0.03045	−0.96
18	483	0.059296	0.001355	0.282371	0.000032	0.282371	−14.20	1.12009	1.26	0.04523	1.98	0.04523	−0.96
19	486	0.052180	0.001216	0.282416	0.000026	0.282416	−12.60	0.91248	1.19	0.03676	1.88	0.03676	−0.96
20	480	0.081259	0.001851	0.282481	0.000027	0.282481	−10.28	0.93926	1.12	0.03855	1.74	0.03855	−0.94
21	476	0.158626	0.003610	0.282735	0.000030	0.282735	−1.33	1.05080	0.79	0.04558	1.17	0.04558	−0.89
22	475	0.135368	0.003280	0.282619	0.000048	0.282619	−5.43	1.68389	0.96	0.07211	1.43	0.07211	−0.90
23	480	0.048808	0.001123	0.282397	0.000026	0.282397	−13.27	0.90869	1.21	0.03650	1.92	0.03650	−0.97
24	476	0.045625	0.001070	0.282423	0.000026	0.282423	−12.33	0.89822	1.17	0.03605	1.86	0.03605	−0.97
25	474	0.060781	0.001419	0.282454	0.000027	0.282454	−11.25	0.93088	1.14	0.03774	1.80	0.03774	−0.96

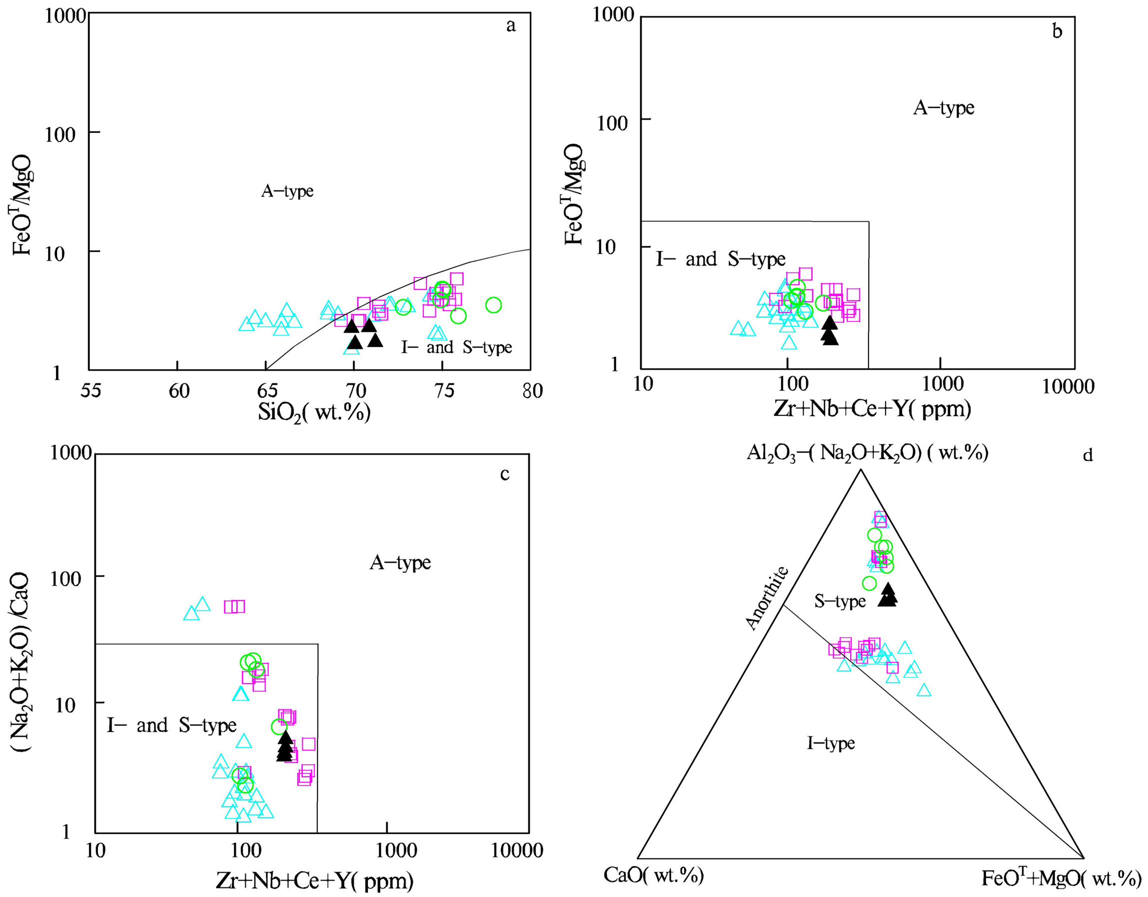

Fig. 9 Geochemical data for the Early Paleozoic granites in the Baoshan block, SW China, plotted on **a** the FeO^T/MgO vs. SiO$_2$ diagram (Eby 1990), **b** the FeO^T/MgO vs. Zr + Nb + Ce + Y diagram (Whalen et al. 1987), **c** the (Na$_2$O + K$_2$O)/CaO vs. Zr + Nb + Ce + Y diagram (Whalen et al. 1987), and **d** the [Al$_2$O$_3$–(K$_2$O + Na$_2$O)]–CaO–(FeO^T + MgO) diagram(Chappell and White 1974). Symbols are the same as those in Fig. 3

kbar (Douce 1999). Granitic melts that are hotter (> 875 °C) have low Al$_2$O$_3$/TiO$_2$ ratios of less than 100, whereas melts that are cooler (< 875 °C) have high Al$_2$O$_3$/TiO$_2$ ratios of more than 100 (Sylvester 1998). The average Al$_2$O$_3$/TiO$_2$ ratio of the granites is 78, indicating that the magma temperature was higher than 875 °C. In the Pb vs. Ba diagram, the samples are plotted in the high temperature field (Fig. 13b). As a result, magma should have been created in an extensional tectonic setting of high temperature and low pressure (HTLP). Experimental simulation investigations have demonstrated that the heat required to partially melt the metasedimentary rocks at this temperature range under normal geothermal gradients is certainly insufficient at crust depths of 16.5 km (Sylvester 1998; Clemens 2003). As was previously indicated, the slight mantle melts are likely what provided the extra heat for crustal anatexis in the peraluminous granites from the Nansa area, which were produced mostly from partial melting of old metasedimentary rocks.

Many tectonic scenarios have been presented, including East Gondwana's final assembly (Meert and Voo 1997), crustal extension in a non-arc environment (Miller et al. 2001; Collins et al. 2014), and an Andean-type orogeny (Cawood et al. 2007). The Nb vs. Y and Rb vs. Y + Nb graphs (Figs. 14a and b) show that the Nansa granites fall within the fields of volcanic arc granite and syn-collisional granite, indicating that arc-related magmatism most likely existed in the Baoshan block in the Early Paleozoic. Moreover, these granites' geochemical traits reflect those of leucogranites that were deposited in collisional orogens elsewhere, including in the high Himalaya, which reduces the likelihood of crustal extension in non-arc environments (Guo and Wilson 2012; Wang et al. 2012). The Himalayan orogen, which includes NW India, the southern Tibetan Plateau, and central Nepal's Himalaya, has all been linked to Cambro-Ordovician deformation and metamorphism (Argles et al. 1999). In the Lhasa (Chen et al. 2022), Tethyan Himalaya (Garzanti et al. 1986), and Baoshan (Dong 2016) blocks, Cambro-Ordovician angular unconformity was extensively developed. Furthermore, the bulk of Early Paleozoic magmatic rocks were deposited within peri-Gondwanan continental blocks at a time that was far

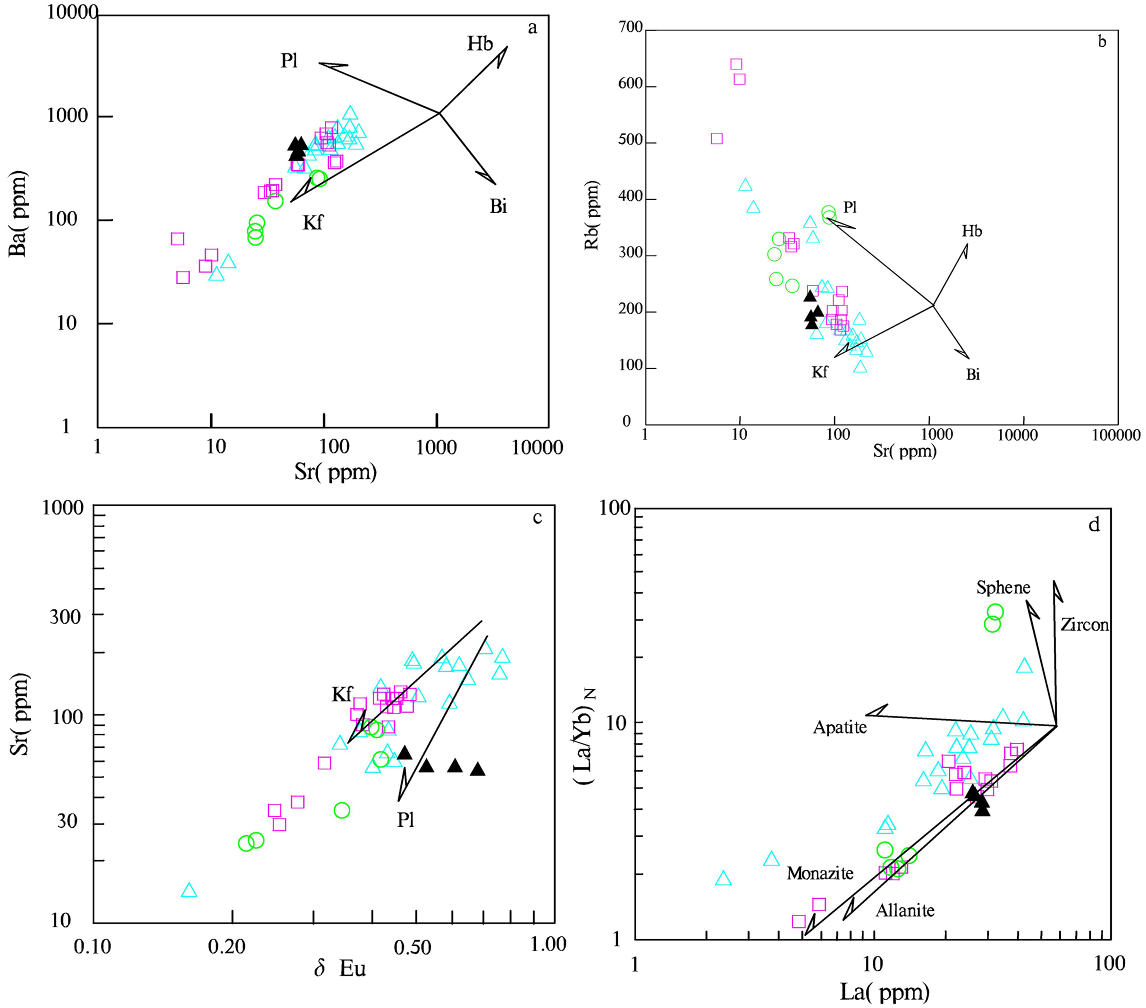

Fig. 10 Sr versus Ba (**a**), Sr versus Rb (**b**),Eu*/Eu versus Sr (**c**) and $(La/Yb)_N$ vs. La diagrams for the Early Paleozoic granites in the Baoshan block, SW China. Kf, Pl, Bi and Hb note the removal of K-feldspar, plagioclase, biotite and hornblende during magma evolution, respectively (Wang et al. 2013). Symbols are the same as those in Fig. 3

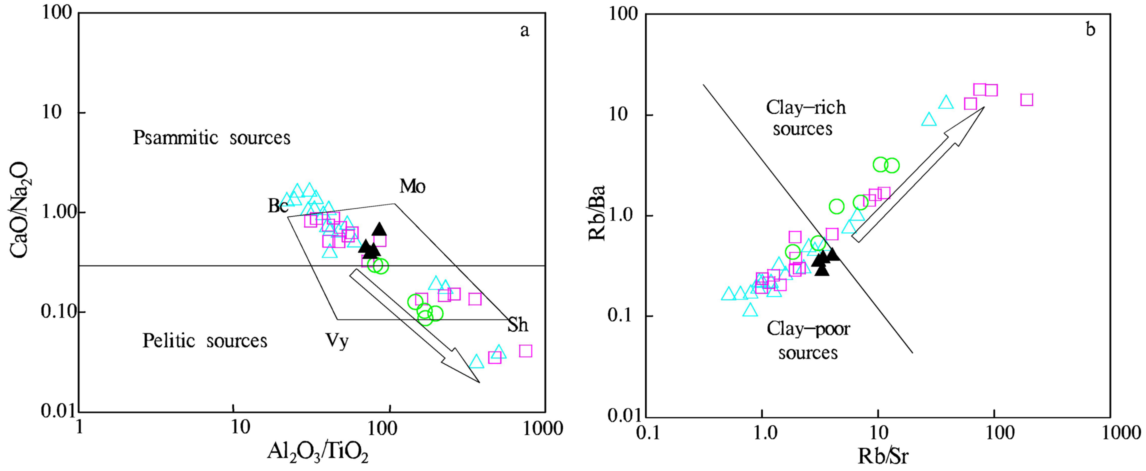

Fig. 11 **a** CaO/Na_2O vs. Al_2O_3/TiO_2 and Rb/Ba vs. Rb/Sr diagrams of the Early Paleozoic granites in the Baoshan block, SW China (Sylvester 1998). Be-Bethanga intrusion in Lachlan fold belt, Australia; Mo-Moschumandl intrusion in Alps oronenic belt; Vy-Vysoky-Kamen intrusion in Hercynian orogenic belt; Sh-Shisga Pangma intrusion in Himalaya orogenic belt. Symbols are the same as those in Fig. 3

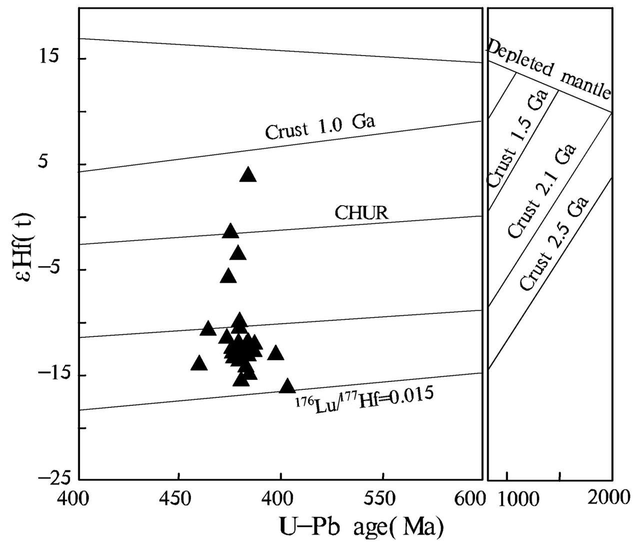

Fig. 12 Plots of ε_{Hf}(t) vs. U–Pb ages of the Nansa granites in the Baoshan block, SW China

later than the final assembly of Gondwana (ca. 570–520 Ma), hence eliminating the likelihood of Gondwana's final assembly (Meert 2003; Cawood et al. 2007). In conclusion, the evidence implies that the Early Palaeozoic S-type granites in the Baoshan block were formed in an HTLP extensional tectonic context as a result of Andean-type orogeny rather than in the final assembly of Gondwana or in crustal extension in a non-arc environment.

5.4.2 Tectonic model

The tectonic contexts in which the peraluminous granites may have developed include continental arcs, back-arcs, syncollisional environments, and post-collisional environments (Collins and Richards 2008; Li et al. 2016a). Earlier research revealed that proto-Tethyan slab rollback (> 500 Ma), slab breakoff (ca. 500–490 Ma), lithospheric thickening (ca. 490–475 Ma), and lithospheric delamination (ca. 475–460 Ma) were the causes of the long-lasting Early Paleozoic peraluminous magmatism in the Baoshan block (Zhu et al. 2012, 2013; Dong et al. 2013a; Li et al. 2016a). Around 450 Ma marked the end of proto-Tethyan accretionary orogenesis, when magmatism ceased to occur (Li et al. 2016a). According to the aforementioned study, the Nansa granites were created in an extensional tectonic setting of high temperature and low pressure (HTLP), in contradiction to previous analyses. For a deeper description of their tectonic setting, the regional geology must be taken into account.

Prior researches has described a phase of Early Paleozoic magmatism in the Baoshan block that lasted in two distinct periods, 502–486 and 476–448 Ma (Dong et al. 2013a, b). Both phases had asthenosphere material upwelling, and phases I and II correlate to the proto-Tethyan oceanic slab breakoff and the lithospheric delamination, respectively (Hu et al. 2015). During the two eras of magmatism, the tectonic setting thickened and shortened, and there was almost no upwelling of mantle material or granite, which was consistent with the absence of Early Ordovician strata (ca. 490–470 Ma) and the existence of Late Ordovician strata in the Baoshan block (Cai et al. 2013). Given the facts presented above, this

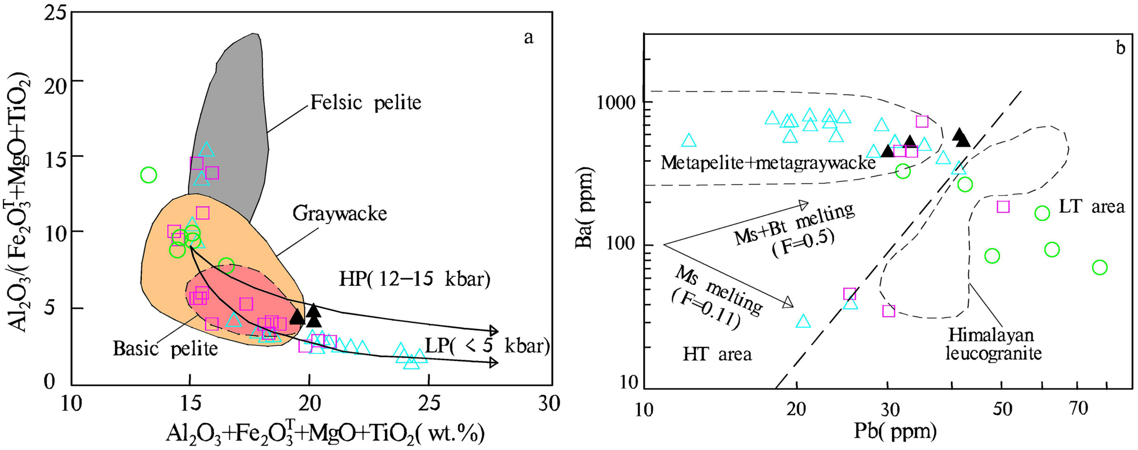

Fig. 13 Diagrams showing P–T conditions of magma generation in the Baoshan block, SW China. **a** Ba versus Pb (Finger and Schiller 2012); **b** [Al_2O_3/($Fe_2O_3^T$ + MgO + TiO_2)] versus (Al_2O_3 + $Fe_2O_3^T$ + MgO + TiO_2), and melts produced by experiments during different pressure conditions(Douce 1999). The thick solid lines represent the reaction curves: HP (P = 12–15 kbar) and LP ($P \leq 5$ kbar). Abbreviations: Bt, biotite; F, weight fraction of melt relative to original parent; HT, high temperature; LT, low temperature; MS, muscovite; LP, low pressure. Symbols are the same as those in Fig. 3

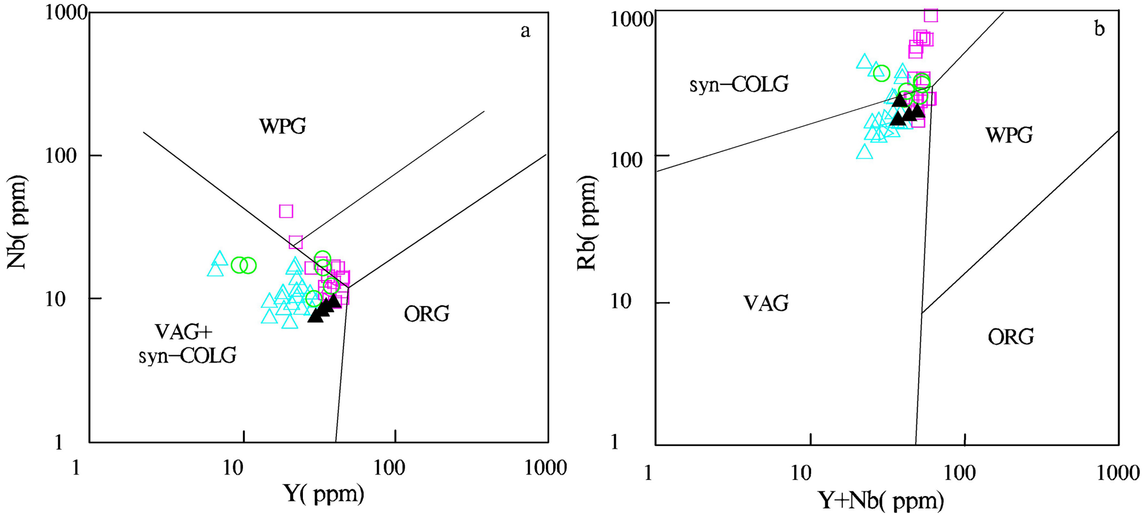

Fig. 14 Trace element discrimination diagrams for the Early Paleozoic granites in the Baoshan block, SW China (Pearce et al. 1984). VAG-volcanic arc granites; ORG-ocean ridge granites; WPG-within-plate granites; SYN-COLG-syn-collisional granites. Symbols are the same as those in Fig. 3

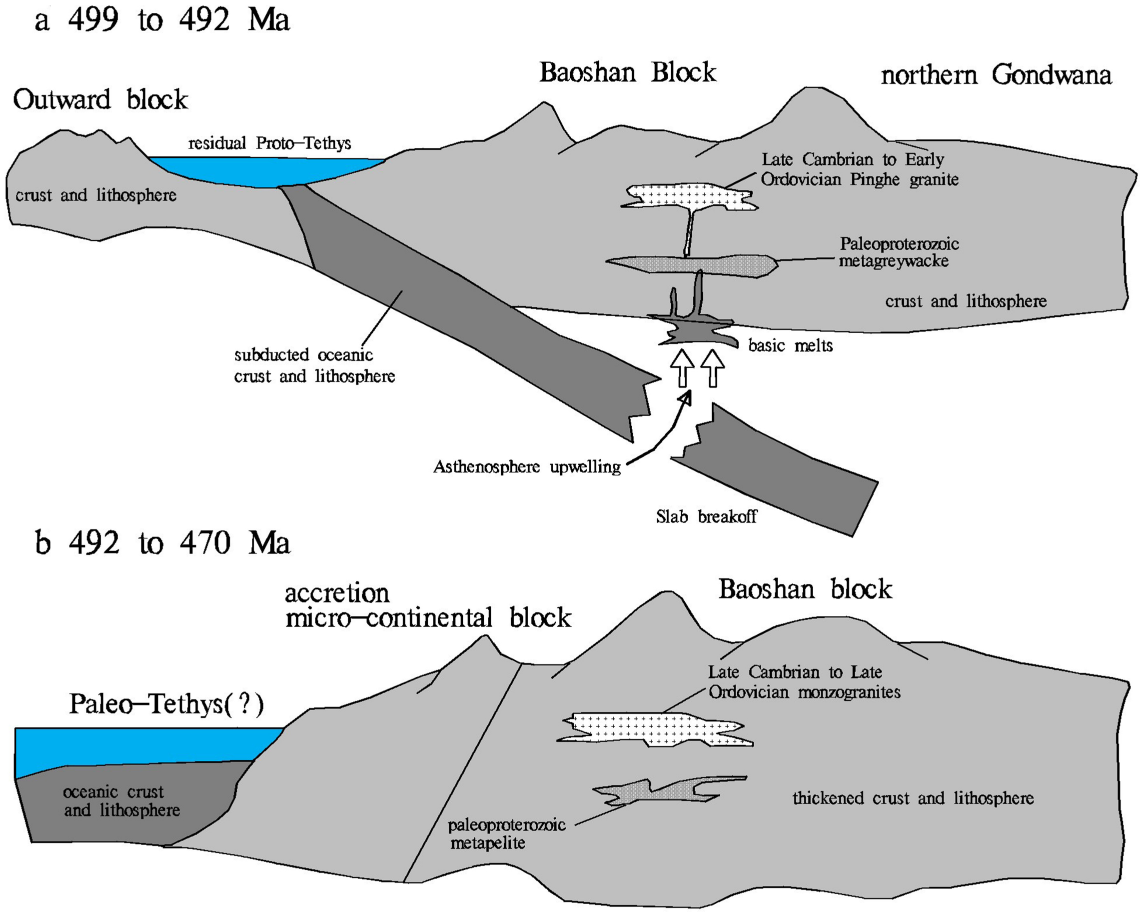

Fig. 15 Schematic illustrations showing the petrogenesis and tectonic setting for the late Cambrian to Early Ordovician magmatism along the East Gondwana margin (Zhao et al. 2017)

article also recognizes that the lithospheric thickening occurred between 490 and 475 Ma, causing the volcano-sedimentary sequence of the Gongyanghe Group to fold (Zhu et al. 2012; Li et al. 2016a) and the local formation of peraluminous igneous rocks (such as this article) in the Baoshan block. In contrast to the tectonic background of the lithosphere's thickening and shortening, this research postulates that an expanding environment may exist in certain localities, causing the crust to melt and decompress, mantle-derived elements to mix, and a small amount of peraluminous granite to developed (Fig. 15). Seldom occurring peraluminous granite of this type corresponds to the paucity of intrusive rocks between 490 and 470 Ma.

Following the accretion of the outer block, the slab breakoff of the subducting proto-Tethyan oceanic lithosphere occurred at 499–492 Ma (Fig. 15a). The slab breakoff caused partial melting of the overlaying lithosphere mantle wedge, resulting in parental basaltic melts for the ca. 499 Ma metabasalts in the Gongyanghe Group's uppermost section. Such mantle-derived magmas could have also contributed heat and possibly material for crustal anatexis, resulting in the formation of enormous peraluminous granites like the main body of the Pinghe pluton (Thibault et al. 2011; Zhu et al. 2012). At roughly 492–475 Ma, the lithospheric thickening occurred, producing the folding of the Gongyanghe Group's volcano-sedimentary sequence and the local formation of peraluminous granitic rocks in the crust, such as the Nansa granite (Fig. 15b) (Von Blanckenburg and Davies 1995; Dong et al. 2013b; Zhao et al. 2017). The long-lived Cambrian-Ordovician peraluminous granitic magmatism in the Baoshan block was formed according to hypothesized sequential tectonic models; however, these models need more support from geological, geochronological, and geochemical research on the Early Paleozoic geological records.

6 Conclusions

The Nansa intrusion in the Baoshan block was emplaced during the Early Ordovician at ca. 480 Ma, and the intrusive rocks are high-K, calc-alkaline, strongly peraluminous granites with almost crustal isotopic characteristics. The Early Ordovician granitic magma in the Baoshan block experienced crystallization fractionation and could be derived from the partial melting of metagreywacke with minor mantle melts.

The Early Palaeozoic S-type granites from Nansa area were generated in a high-temperature and low-pressure (HTLP) extensional tectonic setting, which resulted from Andean-type orogeny instead of the final assembly of Gondwana or crustal extension in a non-arc environment.

In certain places, an expanding environment may exist in opposition to the tectonic backdrop of the lithosphere's thickening and shortening, leading the crust to melt and decompress, mantle-derived materials to mix, and a small quantity of peraluminous granite to emerge.

Authors' contributions J-JZ conceived of the presented idea and developed the theoretical formalism after wrote the manuscript. C-DL provision of samples and preparation of regional geological maps. YZ, TC and H-LL helped complete sample processing and testing. C-LM contributed to the final version of the manuscript.

Funding This research is funded by the National Natural Science Foundation of China (2019M653840XB) and the National Natural Science Foundation of China (41972043 and 42062006).

Availability of data and material The results from our study is our original unpublished work and it has not been submitted to any other journal for reviews.

Code availability There are no software application or custom code.

Declarations

Conflict of interest On behalf of all authors, the corresponding author states that there is no conflict of interest.

Ethics approval This manuscript we wish to be considered for publication in "ACTA Geochimica". No conflict of interest exits in the submission of this manuscript, and manuscript is approved by all authors for publication. I would like to declare on behalf of my co-authors that the work described was original research that has not been published previously, and not under consideration for publication elsewhere, in whole or in part. All the authors listed have approved the manuscript that is enclosed.

References

Amelin Y, Lee DC, Halliday AN (2000) Early-middle archaean crustal evolution deduced from Lu-Hf and U-Pb isotopic studies of single zircon grains. Geochim Cosmochim Acta 64:4205–4225

Argles TW, Prince CI, Foster GL, Vance D (1999) New garnets for old? Cautionary tales from young mountain belts. Earth Planet Sci Lett 172:301–309

Bonin B (2007) A-type granites and related rocks: evolution of a concept, problems and prospects. Lithos 97:1–29

Bruce W, Chappell A, Colleen J, Bryant A, Doone W (2012) Peraluminous I-type granites. Lithos 153:142–153

Cai Z, Xu Z, Duan X, Li H, Cao H, Huang X (2013) Early Paleozoic orogenic event in western Yunnan, southeast margin of Qinghai-Tibet Plateau. Acta Petrologica Sinica 29:2123–2140

Cawood PA, Buchan C (2007) Linking accretionary orogenesis with supercontinent assembly. Earth-Sci Rev 82:217–256

Cawood PA, Johnson M, Nemchin AA (2007) Early Palaeozoic orogenesis along the Indian margin of Gondwana: tectonic response to Gondwana assembly. Earth Planet Sci Lett 255:70–84

Chappell BW, White A (1974) Two contrasting granite type. Pacific Geol 8:173–174

Chappell BW, White AJR (1992) I- and S-type granites in the Lachlan Fold Belt. Trans Roy Soc Edinburgh Earth Sci 83:1–26

Chen JS (1987) Discussion on age division and isotopic age selection of granitoids in western Yunnan. Yunnan Geol 6:101–113

Chen F, Li XH, Wang XL, Li QL, Siebel W (2008) Zircon age and Nd–Hf isotopic composition of the Yunnan Tethyan belt, southwestern China. Int J Earth Sci 96:1179–1194

Chen Y, Zhang Z, Chen X, Palin RM, Tian Z, Shao Z, Qin S, Yuan Y (2022) Neoproterozoic and Early Paleozoic magmatism in the eastern Lhasa terrane: implications for Andean-type orogeny along the northern margin of Rodinia and Gondwana. Precambr Res 369:106–520

Clemens JD (2003) S-type granitic magmas-petrogenetic issues, models and evidence. Earth Sci Rev 61:1–18

Collins W, Richards SW (2008) Geodynamic significance of S-type granites in circum-Pacific orogens. Geology 36:559–562

Collins AS, Clark C, Plavsa D (2014) Peninsular India in Gondwana: the tectonothermal evolution of the Southern Granulite Terrain and its Gondwanan counterparts. Gondwana Res 25:190–203

Cong F, Lin SL, Tang HF, Xie T, Li ZH, Zhou GF, Pen ZM, Liang T (2010) Elements and Hf isotope compositions and U Pb age of igneous zircons from the triassic Granite in Lianghe, Western Yunnan. Acta Petrologica Sinica 84:1155–1164

Deng J, Wang C, Bagas L, Selvaraja V, Jeon H, Wu B, Yang L (2017) Insights into ore genesis of the Jinding Zn-Pb deposit, Yunnan Province, China: Evidence from Zn and in-situ S isotopes. Ore Geol Rev 90:943–957

Dong ML, Dong GC, Mo XX, Zhu DC, Nie F, Xf X, Wang X, Hu ZC (2012) Chronology, geochemistry and significance of Early Paleozoic granites in Baoshan Block, western Yunnan. Acta Petrologica Sinica 28:1453–1464

Dong ML, Dong GC, Mo XX, Santosh M, Zhu DC, Nie F, Yu JC, Wang P, Luo W (2013a) Meso-cenozoic magmatism and its tectonic implications in Baoshan Block, western Yunnan. Acta Petrologica Sinica 29:3901–3913

Dong ML, Dong GC, Mo XX, Santosh M, Zhu DC, Yu JC, Nie F, Hu ZC (2013b) Geochemistry, zircon U-Pb geochronology and Hf isotopes of granites in the Baoshan Block, Western Yunnan: implications for Early Paleozoic evolution along the Gondwana margin. Lithos 179:36–47

Dong ML (2016) Study of magmatism in Tengchong-Baoshan Block, western Yunnan and its tectonic implications. China University of Geosciences (Beijing)

Douce AEPP (1999) What do experiments tell us about the relative contributions of crust and mantle to the origin of granitic magmas? Geol Soc Lond Spec Publ 168:55–75

Eby GN (1990) The A-type granitoids: a review of their occurrence and chemical characteristics and speculations on their petrogenesis. Lithos 26:115–134

Finger F, Schiller D (2012) Lead contents of S-type granites and their petrogenetic significance. Contrib Miner Petrol 164:747–755

Frost BR, Barnes CG, Collins WJ, Arculus RJ, Ellis DJ, Frost CD (2001) A geochemical classification for granitic rocks. J Petrol 42:2033–2048

Garzanti E, Casnedi R, Jadoul F (1986) Sedimentary evidence of a Cambro-Ordovician orogenic event in the Northwestern Himalaya. Sed Geol 48:237–265

Guo SS, Li SG (2009) Petrochemical characteristics of leucogranite and a case study of Bengbu leucogranites. Chin Sci Bull English Edition 54:1923–1930

Guo Z, Wilson M (2012) The Himalayan leucogranites: constraints on the nature of their crustal source region and geodynamic setting. Gondwana Res 22:360–376

Hoskin PWO, Schaltegger U (2018) The composition of zircon and igneous and metamorphic petrogenesis. Rev Mineral Geochem 53:27–62

Hu PY, Zhai QG, Jahn BM, Wang J, Li C, Lee HY, Tang SH (2015) Early Ordovician granites from the South Qiangtang terrane, northern Tibet: implications for the Early Paleozoic tectonic evolution along the Gondwanan proto-Tethyan margin. Lithos 220:318–338

Jerome G, Paul K, George EG, Lin D (2012) U-Pb geochronology of basement rocks in central Tibet and paleogeographic implications. J Asian Earth Sci 43:23–50

Jin SC, Zhuang FL (1988) Study of melting inclution in granites at Longling in Luxi area. J Kunming Inst Technol 13:1–15

Kawakami T, Nakano N, Higashino F, Hokada T, Hirata T (2014) U-Pb zircon and CHIME monazite dating of granitoids and high-grade metamorphic rocks from the Eastern and Peninsular Thailand – a new report of Early Paleozoic granite. Lithos 200:64–79

Kinny PD (2003) Lu-Hf and Sm-Nd isotope systems in zircon. Rev Mineral Geochem 53:327–341

Li XW, Mo XX, Zhao ZD, Zhu DC (2010b) A discussion on how to discriminate A-type granite. Geol Bull China 29:278–285

Li GZ, Su SG, Lei WY, Duan XD (2011) Precise ID-TIMS zircon U-Pb age and whole-rock geochemistry of the Nanlinshan mafic intrusion in the southern Lancangjiang arc terrane, Sanjiang area, SW China. Earth Sci Front 18:206–212

Li GJ, Wang QF, Huang YH, Chen FC, Dong P (2015a) Discovery of Hadean-Mesoarchean crustal materials in the northern Sibumasu block and its significance for Gondwana reconstruction. Precambr Res 271:118–137

Li XW, Mo XX, Huang XF, Dong GC, Yu XH, Luo MF, Liu YB (2015b) U-Pb zircon geochronology, geochemical and Sr-Nd-Hf isotopic compositions of the early Indosinian Tongren Pluton in West Qinling: petrogenesis and geodynamic implications. J Asian Earth Sci 97:38–50

Li YG, Wang SS, Liu MW, Meng E, Wei XY, Zhao HB, Jin MQ (2015c) U-Pb dating study of Baddeleyite byLA-ICP-MS: technique and application. Acta Geol Sin 89:2400–2418

Li GJ, Wang QF, Huang YH, Gao L, Yu L (2016a) Petrogenesis of middle Ordovician peraluminous granites in the Baoshan block: Implications for the Early Paleozoic tectonic evolution along East Gondwana. Lithos 245:76–92

Li WC, Pan GT, Hou ZQ (2010a) Archipelagic-basin, forming collision theory and prospecting techniques along the Nujiang-Lancangjiang-Jinshajiang Area in Southwestern China. Geological Publishing House

Li YJ, Wei JH, Santosh M, Tan J, Fu LB, Zhao SQ (2016b) Geochronology and petrogenesis of Middle Permian S-type granitold in southeastern Guangxi Province, South China: implications for closure of the eastern Paleo-Tethys. Tectonophysics: Int J Geotect Geol Phys Interior Earth 682:1–16

Lin YL, Yeh MW, Lee TY, Chung SL, Iizuka Y, Charusiri P (2013) First evidence of the Cambrian basement in Upper Peninsula of Thailand and its implication for crustal and tectonic evolution of the Sibumasu terrane. Gondwana Res 24:1031–1037

Liu Y, Hu Z, Gao S, Günther D, Xu J (2008) In situ analysis of major and trace elements of anhydrous minerals by LA-ICP-MS without applying an internal standard. Chem Geol 257:34–43

Liu S, Hu RZ, Gao S, Feng CX, Huang ZL, Lai SC, Yuan HL, Liu XM, Coulson IM, Feng GY, Wang T, Qi YQ (2009) U-Pb zircon, geochemical and Sr-Nd-Hf isotopic constraints on the age and origin of Early Palaeozoic I-type granite from the Tengchong-Baoshan Block, Western Yunnan Province, SW China. J Asian Earth Sci 36:168–182

Liu W, Wang BD, Yang XY, Yuan SH, Liu H, Liao Zl (2018) Geochronology, Geochemistry, and Sr-Nd-Hf Isotopes of the Balazha Ore-Bearing Porphyries: Implications for Petrogenesis and Geodynamic Setting of Late Cretaceous Magmatic Rocks in the Northern Lhasa Block, Tibet. Acta Geologica Sinica (English Edition) 92: 1739–1752

Ludwig KR (2003) ISOPLOT 3.0: A geochronological Toolkit for Microsoft Excel. Berkeley Geochronology Center Special Publication

Maniar PD, Piccoli PM (1989) Tectonic discrimination of granitoids. Geol Soc Am Bull 101:635–643

Meert JG (2003) A synopsis of events related to the assembly of eastern Gondwana. Tectonophysics 362:1–40

Meert JG, Voo R (1997) The assembly of Gondwana 800–550 Ma. J Geodyn 23:223–235

Meinhold G, Morton AC, Avigad D (2013) New insights into peri-Gondwana paleogeography and the Gondwana super-fan system from detrital zircon U-Pb ages. Gondwana Res 23:661–665

Meng E, Liu FL, Liu PH, Liu CH, Yang H, Wang F, Shi JR, Cai J (2014) Petrogenesis and tectonic significance of Paleoproterozoic meta-mafic rocks from central Liaodong Peninsula, northeast China: evidence from zircon U-Pb dating and in situ Lu-Hf isotopes, and whole-rock geochemistry. Precambr Res 247:92–109

Metcalfe I (2006) Palaeozoic and Mesozoic tectonic evolution and palaeogeography of East Asian crustal fragments: The Korean Peninsula in context. Gondwana Res 9:24–46

Metcalfe I (2013) Gondwana dispersion and Asian accretion: tectonic and palaeogeographic evolution of eastern Tethys. J Asian Earth Sci 66:1–33

Middlemost EAK (1994) Naming materials in the magma/igneous rock system. Earth Sci Rev 37:215–224

Miller C, Thöni M, Frank W, Grasemann B, Klötzli U, Guntli P, Draganits E (2001) The Early Palaeozoic magmatic event in the Northwest Himalaya, India: source, tectonic setting and age of emplacement. Geol Mag 138:237–251

Murphy JB, van Staal CR, Collins WJ (2011) A comparison of the evolution of arc complexes in Paleozoic interior and peripheral orogens: speculations on geodynamic correlations. Gondwana Res 19:812–827

Nie F, Dong GC, Mo XX, Zhu DC, Dong MN, Wang X (2012) Geochemistry, zircon U-Pb chronology of the Triassic granites in the Changning-Menglian suture zone and their implications. Acta Petrologica Sinica 28:1465–1476

Pan GT, Wang LQ, Li RS, Yuan SH, Ji WH, Yin FG, Zhang WP, Wang BD (2012) Tectonic evolution of the Qinghai-Tibet Plateau. J Asian Earth Sci 53:3–14

Pearce JA, Harris NBW, Tindle AG (1984) Trace element discrimination diagrams for the tectonic interpretation of granitic rocks. J Petrol 25:956–983

Prowatke S, Klemme S (2006) Trace element partitioning between apatite and silicate melts. Geochim Cosmochim Acta 70:4513–4527

Pullen A, Kapp P, Gehrels GE, Ding L, Zhang Q (2011) Metamorphic rocks in central Tibet: lateral variations and implications for crustal structure. Geol Soc Am Bull 123:585–600

Quigley MC, Liangjun Y, Gregory C, Corvino A, Sandiford M, Wilson C, Xiaohan L (2008) U-Pb SHRIMP zircon geochronology and T-t-d history of the Kampa Dome, southern Tibet. Tectonophysics 446:97–113

Rudnick RL, Fountain DM (1995) Nature and composition of the continental crust: a lower crustal perspective. Rev Geophys 33:267–309

Shen SZ, Shi GR, Fang ZJ (2002) Permian brachiopods from the Baoshan and Simao Blocks in Western Yunnan, China. J Asian Earth Sci 20:665–682

Shen L, Hu RZ, Shan G, Feng CX, Huang Z, Lai S, Yuan H, Liu X, Coulson IM, Feng G (2009) U-Pb zircon, geochemical and Sr-Nd-Hf isotopic constraints on the age and origin of Early Palaeozoic I-type granite from the Tengchong-Baoshan Block, Western Yunnan Province, SW China. J Asian Earth Sci 36:168–182

Simon I, Nigel H (1993) Geochemical constraints on Leucogranite Magmatism in the Langtang Valley, Nepal Himalaya. J Petrol 34:345–368

Sun SS, McDonough WF (1989) Chemical and isotopic systematics of oceanic basalts: Implications for mantle composition and processes. Geol Soc Lond Spec Publ 42:331–345

Sylvester PJ (1998) Post-collisional strongly peraluminous granites. Lithos 45:29–44

Thibault D, Taras V, Gerya, Dave A (2011) Numerical modelling of spontaneous slab breakoff and subsequent topographic response. Tectonophysics 502:244–256

Vervoort JD, Patchett PJ (1996) Behavior of hafnium and neodymium isotopes in the crust: Constraints from Precambrian crustally derived granites. Geochim Cosmochim Acta 60:3717–3733

Vidal P, Cocherie A, Fort PL (1982) Geochemical investigations of the origin of the Manaslu leucogranite (Himalaya, Nepal). Geochim Cosmochim Acta 46:2279–2292

Von Blanckenburg F, Davies JH (1995) Slab breakoff: a model for syncollisional magmatism and tectonics in the Alps. Tectonics 14:120–131

Wang Q, Chung SL, Li XH, Wyman D, Li ZX, Sun WD, Qiu HN, Liu YS, Zhu YT (2012) Crustal melting and flow beneath Northern Tibet: evidence from Mid-Miocene to quaternary strongly Peraluminous Rhyolites in the Southern Kunlun range. J Petrol 53:2523–2566

Wang YJ, Xing XW, Cawood PA, Lai SC, Xia XP, Fan WM, Liu HC, Zhang FF (2013) Petrogenesis of Early Paleozoic peraluminous granite in the Sibumasu Block of SW Yunnan and diachronous accretionary orogenesis along the northern margin of Gondwana. Lithos 182–183:67–85

Whalen JB, Currie KL, Chappell BW (1987) A-type granites: geochemical characteristics. Contrib Miner Petrol 95:420–436

Wopfner H (1996) Gondwana origin of the Baoshan and Tengchong terranes of west Yunnan. Tectonic Evolut Southeast Asia 106:539–547

Wu FY, Jahn BM, Wilde SA, Lo CH, Yui TF, Lin Q, Ge WC, Sun DY (2003) Highly fractionated I-type granites in NE China (I): geochronology and petrogenesis. Lithos 66:241–273

Xiong CL, Jia XC, Ynag XJ, Luo G, Bai XZ, Huang BX (2012) LA-ICP-MS zircon U-Pb dating and tectonic setting of the Mengmao Ordovician monzogranite in Longling area, western Yunnan. Geol Bull China 31:277–286

Xu Y, Cawood PA, Du Y, Huang H, Wang X (2014) Early Paleozoic orogenesis along Gondwana's northern margin constrained by provenance data from South China. Tectonophysics 636:40–51

Yang XJ, Jia XC, Xiong CL, Bai XZ, Huang BX, Luo G (2012) LA-ICP-MS zircon U-Pb age of metamorphic basic volcanic rock in Gongyanghe Group of southern Gaoligong Mountain, western Yunnan Province, and its geological significance. Geol Bull China 31:264–276

Ye L, Gao W, Cheng ZT, Yang YL, Tao Y (2010) LA-ICP-MS Zircon U-Pb Geochronology and Petrology of the Muchang Alkali Granite, Zhenkang County,Western Yunnan Province, China. Acta Geol Sinica (English Edition) 84: 1488–1499

Zhang YQ, Xie YW, Cheng ZL (1990) Rb-sr isotope age of tin-bearing granites in Sanjiang area. Acta Petrologica Sinica 6:75–81

Zhang LK, Li GM, Santosh M, Cao HW, Dong SL, Zhang Z, Fu JG, Xia XB, Huang Y, Liang W, Zhang ST, Li S (2019) Cambrian magmatism in the Tethys Himalaya and implications for the evolution of the Proto-Tethys along the northern Gondwana margin: a case study and overview. Geol J 54:2545–2565

Zhao SW, Lai SC, Gao L, Qin JF, Zhu RZ (2017) Evolution of the Proto-Tethys in the Baoshan block along the East Gondwana margin: constraints from Early Palaeozoic magmatism. Int Geol Rev 59:1–15

Zhu DC, Zhao ZD, Niu YN, Dilek Y, Wang Q, Ji WH, Dong GC, Sui QL, Liu YS, Yuan HL, Mo XX (2012) Cambrian bimodal volcanism in the Lhasa Terrane, southern Tibet: Record of an Early Paleozoic Andean-type magmatic arc in the Australian proto-Tethyan margin. Chem Geol 328:290–308

Zhu DC, Zhao ZD, Niu YL, Dilek Y, Hou ZQ, Mo XX (2013) The origin and pre-Cenozoic evolution of the Tibetan Plateau. Gondwana Res 23:1429–1454